INTERNATIONAL JOURNAL FOR NUMERICAL METHODS IN FLUIDS
Int. J. Numer. Meth. Fluids 2010; **63**:40–68
Published online 29 April 2009 in Wiley InterScience (www.interscience.wiley.com). DOI: 10.1002/fld.2055

Developing a unified FVE-ALE approach to solve unsteady fluid flow with moving boundaries

A. Naderi[‡], M. Darbandi[*, †, §] and M. Taeibi-Rahni[¶]

Department of Aerospace Engineering, Sharif University of Technology, P.O. Box 11365-8639, Tehran, Iran

SUMMARY

In this study, an arbitrary Lagrangian–Eulerian (ALE) approach is incorporated with a mixed finite-volume–element (FVE) method to establish a novel moving boundary method for simulating unsteady incompressible flow on non-stationary meshes. The method collects the advantages of both finite-volume and finite-element (FE) methods as well as the ALE approach in a unified algorithm. In this regard, the convection terms are treated at the cell faces using a physical-influence upwinding scheme, while the diffusion terms are treated using bilinear FE shape functions. On the other hand, the performance of ALE approach is improved by using the Laplace method to improve the hybrid grids, involving triangular and quadrilateral elements, either partially or entirely. The use of hybrid FE grids facilitates this achievement. To show the robustness of the unified algorithm, we examine both the first- and the second-order temporal stencils. The accuracy and performance of the extended method are evaluated via simulating the unsteady flow fields around a fixed cylinder, a transversely oscillating cylinder, and in a channel with an indented wall. The numerical results presented demonstrate significant accuracy benefits for the new hybrid method on coarse meshes and where large time steps are taken. Of importance, the current method yields the second-order temporal accuracy when the second-order stencil is used to discretize the unsteady terms.

Received 27 February 2008; Revised 24 February 2009; Accepted 26 February 2009

KEY WORDS: finite-volume–element method; arbitrary Lagrangian–Eulerian approach; physical influence upwinding scheme; moving boundary; second-order time accuracy; hybrid mesh

1. INTRODUCTION

There are many different approaches for solving fluid flow problems with moving boundaries and moving meshes. A few of them can be counted as the integrated space–time [1, 2], the

*Correspondence to: M. Darbandi, Department of Aerospace Engineering, Sharif University of Technology, P.O. Box 11365-8639, Tehran, Iran.
†E-mail: darbandi@sharif.edu
‡Ph.D. Candidate.
§Professor.
¶Associate Professor.

arbitrary Lagrangian–Eulerian (ALE) [3, 4], and the boundary-transformation [5, 6] approaches. Among them, the ALE approach seems to be more attractive because of its high capabilities in mesh transformation. The ALE method can be viewed from different perspectives. From the first perspective, the incorporation of ALE capabilities with finite-volume (FV) method increases the strength. However, using an ALE-FV method, two important questions are how to treat the convection and diffusion fluxes at the cell faces on the moving ALE frame and how to couple the mass and momentum conservation laws on the moving ALE frame. For example, Demirdzic and Peric [3] developed an FV method to treat fluid flow in arbitrarily shaped domains with collocated-grid arrangement. They employed a central difference scheme to treat the diffusion fluxes and a central difference scheme modified by an upwind correction term to treat the convection fluxes. The coupling of the continuity and momentum equations was achieved via using the SIMPLE algorithm. Zhao and Forhad [7] also used a cell-centered FV method to model the solid–fluid interaction. They utilized an upwind strategy along the characteristic direction benefiting from the third-order MUSCL interpolation. They considered the artificial compressibility concept to couple the continuity and momentum equations. Ahn and Kallinderis [4] also extended a cell-centered FV method on hybrid unstructured meshes. They used a node-centered median dual scheme and the volume-averaged velocity gradient at the edge midpoint to treat the convection and diffusion fluxes, respectively. They applied the artificial compressibility method to couple the pressure and velocity fields.

From the second perspective, the ALE can be viewed as a mesh movement strategy. The split ALE approach has three major steps. First, the governing equations are numerically solved in the Lagrangian step. Second, an improved mesh is constructed, i.e. rezoning. Third, the results of solving flow on the Lagrangian mesh are transformed to the improved mesh, i.e. remapping. Indeed, the strengths and weaknesses of the split ALE approach stem from the Lagrangian step. This provides vital information about the underlying flow, which can be used by the mesh movement algorithms. This can be used to improve the accuracy and can help a lot with treating the moving boundaries and material interfaces. However, the downside is that it may lead to ill robustness. It is because a cell could invert or the time step could collapse in the Lagrangian step before it can be fixed by the mesh movement algorithm during the advection step or rezone/remap steps. An unsplit scheme can clearly avoid the latter defection. However, it can suffer badly if a boundary is moving rapidly; therefore, special procedures are then required to handle this as it is the concern of this paper. Moreover, the ALE rezoning and remapping steps are computationally expensive and additional treatments in removing or limiting them can effectively enhance the efficiency of a standard ALE approach. For example, Zhang *et al.* [8, 9] developed a dynamic hybrid grid approach to improve their mesh with minimal local rezoning and remapping requirements. They used the spring-analogy method to deform their triangular meshes. Alternatively, one may use the Laplace method to deform the mesh [10]. In this method, the new x and y locations for each node can be found via solving two Laplace equations in the x and y directions, respectively. The new location is eventually determined using an average of the neighboring node locations. The main disadvantage of the Laplace method is that the mesh may be folded near the concave boundaries, and this consequently needs suitable treatment.

From the third perspective, two challenging issues in the ALE approach are the time accuracy achievement and the satisfaction of the geometric conservation law (GCL) during the time advancement. For example, Fourestey and Piperno [11] used the second-order backward time stencil in their ALE approach. Using this stencil in addition to the construction of the characteristic paths in a grid relative velocity field, they showed that their ALE formulation would result in the second-order

DOI: 10.1002/fld

time accuracy. Indeed, there are basic requirements in the finite-element (FE) and FV methods to satisfy the GCL. To achieve the second-order time accurate solution, Koobus and Farhat [12] and Geuzaine *et al.* [13] applied semi-discretized form of the unsteady conservation laws in the FE and FV contexts. They showed that the satisfaction of the GCL is not a necessary condition to achieve the desirable temporal accuracy in their time-integrator scheme. They indicated that the first-order time accuracy may be inevitably reached if the time-averaging is not employed properly. They also showed that the time-averaging would be effective in satisfying or dissatisfying the GCL. They finally concluded that the time accuracy would not affect the GCL and vice versa.

Considering the above three important perspectives in developing an ALE approach, we would like to elaborate the contributions of this study to each perspective separately. From the first perspective and as a novel work, we collect the advantages of ALE, FV, and FE methods within a unified algorithm to solve the unsteady incompressible flow in domains with moving mesh and/or moving boundary more robustly. The essence of the idea returns to a basic pressure-based finite-volume–element (FVE) method [14, 15], which is capable of solving fluid flow in domains without moving boundary and/or mesh movements. There are several benefits behind incorporating this FVE method with the ALE approach. First and contrary to past FV investigations, we do not use mathematical-based statements to approximate the convection fluxes at the moving cell faces. We alternatively apply a new upwinding strategy in the streamwise direction to treat these fluxes. The taken strategy is known as a physical-influence or pressure-weighted upwinding scheme [14, 15]. In this study, the original pressure-weighted scheme is extended to treat the convection terms at moving cell faces quite physically. Second, the incorporation of the FE method allows treating very complex solution domains, with arbitrary boundary movements and mesh deformations, very robustly. Furthermore, the use of FE shape functions simplifies the treatments of pressure and diffusion terms at the moving cell faces. Third, to couple the pressure and velocity fields in our collocated moving grids, we utilize the basic idea introduced by Rhie and Chow [16] and its extension suggested by Darbandi and Bostandoost [17], and extend them to moving FVE-ALE grids. From the second perspective, we benefit from the hybrid grid distributions and moving mesh function nearby the wall boundary nodes to reduce the computational cost. Back to our past experience in solving flow on stationary hybrid grids [18, 19], the use of hybrid grids in our Laplace-based method avoids generating tangled elements close to the deformed boundaries even taking very large boundary deformation stages. In other words, the use of hybrid grids reduces the shortcomings of the Laplace method and results in higher performances in mesh movement and lower costs in computations. From the third perspective and the GCL point of view, the use of FV method allows satisfying the GCL in our non-stationary meshes, effectively. The satisfaction is achieved in an explicit manner. From the accuracy point of view, the current unified FVE-ALE strategy guarantees the second-order time accurate solutions. We will show that the current extended algorithm is sufficiently robust and remarkably accurate without employing any type of dissipation term and/or damping function.

2. MESH MOVEMENT STRATEGY

Back to the past experiences, there are two basic choices in selecting the element shape for 2D FE analysis. They are quadrilateral and triangular shapes. Both of these shapes can simultaneously appear in a hybrid mesh [18]. In the flow fields with moving boundary or deformable mesh, the use of a hybrid mesh is very advantageous [8, 9]. First, it uses the flexibility of unstructured triangular

DOI: 10.1002/fld

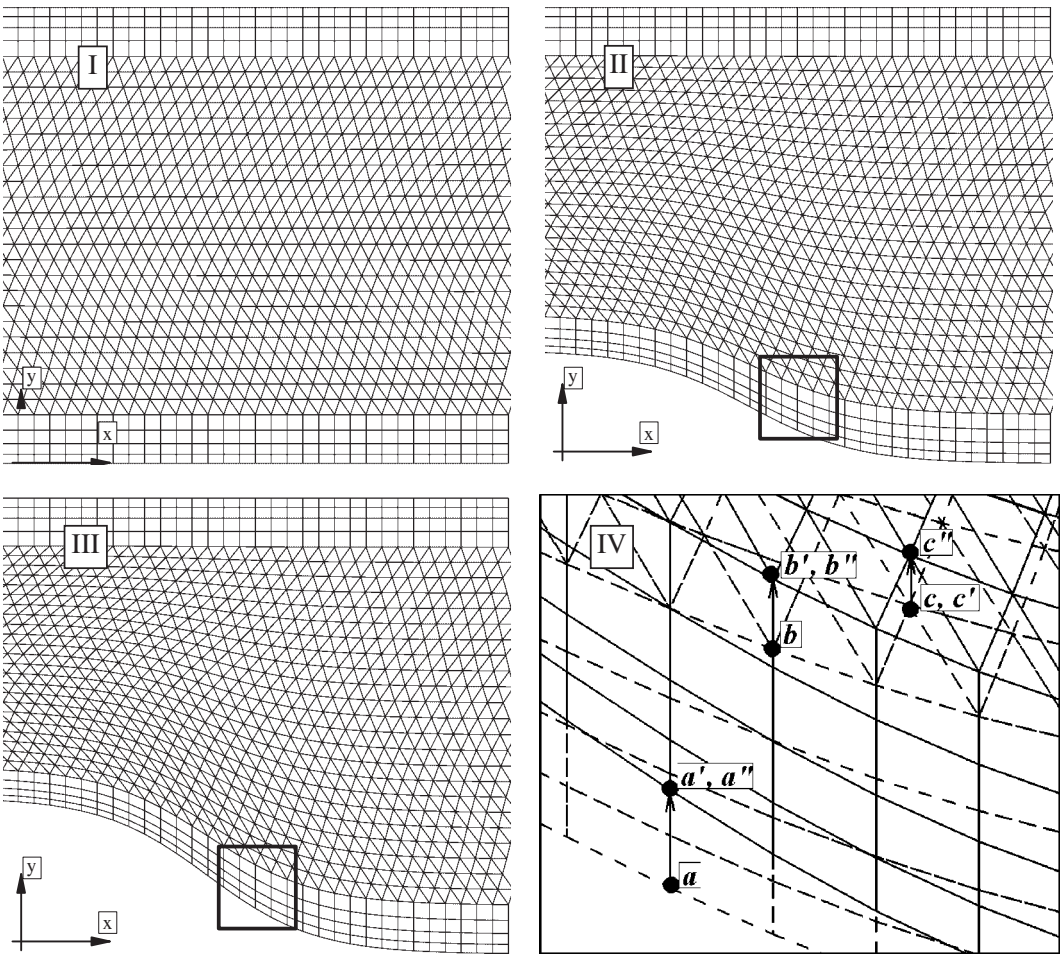

Figure 1. The grid deformation close to the bottom indented wall in a channel.

elements in domains with highly distorted blocks, where mesh clustering is required. Second, it benefits from the advantages of placing quadrilateral elements beside the solid boundaries, where the boundary layer plays an important role on the flow field solution. Figure 1 shows part of a channel, whose bottom wall is oscillating with time. The details of this test case are provided in Section 6. The figure presents three mesh plots of I, II, and III in the channel at three different time steps. Frame I shows the mesh before wall movement. Frames II and III show the mesh before and after one specific time step during boundary movement. The bottom wall reaches to its ultimate upper position during this time step. Frame IV magnifies the details of mesh movement from frame II to III in the shown square. The dashed lines and solid lines in frame IV present the mesh in frames II and III, respectively. As is seen, nodes a, b, and c are initially located on the cell vertices of the grid in frame II. Nodes a'', b'', and c'' are the same nodes after mesh movement shown in frame III. Nodes (a, a'') and (b, b'') are, respectively, located on the lower and upper limits of the block of quadrilateral elements, while nodes c and c'' are located in the

DOI: 10.1002/fld

block of triangular elements. The mesh movement is performed in two stages. First, the nodes on the quadrilateral elements are moved, while the triangular elements are stationary, see nodes a', b', and c'. Second, the nodes on the triangular elements are moved suitably, while the quadrilateral elements are stationary.

According to Figure 1, the coordinates of the new nodes, i.e. x_{new} and y_{new}, on the indented wall are obtained from the moving functions of $(x_I+(1-\kappa_1 x_I)x_w)$ and $(y_I+(1-\kappa_2 y_I)y_w)$, where the subscript I denotes the node location in mesh I, the subscript w denotes the coordinate of the node at the wall, and κ_1 and κ_2 are two constants to control the amount of boundary movements in the x and y directions, respectively. Using these moving functions, the quadrilateral elements in the lower block are suitably moved to their new positions, albeit $x_w=0$ in our indented wall case. The upper boundary of the lower block is the lower boundary of the upper block, where unstructured triangular elements are distributed. Next, we use the Laplace method and obtain the new locations of nodes only in the upper block. We solve two sets of Laplace equations in the x and y directions to obtain x_{new} and y_{new} of the moving nodes. Eventually, the location of each node is obtained as an average of the locations of its neighboring nodes as follows:

$$x_{new}=\sum_{nei=1}^{N_{nei}} x_{nei} \Big/ N_{nei}, \quad y_{new}=\sum_{nei=1}^{N_{nei}} y_{nei} \Big/ N_{nei} \tag{1}$$

where N_{nei} is the number of neighboring nodes and x_{nei} and y_{nei} are their x and y positions. The above relations are iteratively employed for all moving nodes at each time step.

The grid movement strategy is slightly different in external flow applications. We describe it briefly for a transversely oscillating cylinder placed in a crossflow. The details of this test case are provided in Section 6. We divide the solution domain into three blocks, see Figure 2. Block 1 includes nodes located on the cylinder face and nearby it. Block 2 involves nodes located on the inlet, outlet, and free stream boundaries and nearby them. The rest of the mesh is block 3. The elements in blocks 1 and 2 are hybrid, while those in block 3 are triangular. All the nodes in block 1 move with the cylinder motion and have zero relative velocity with respect to the cylinder. However, the nodes in block 2 do not move. Consequently, we need mesh movement for the unstructured triangular block 3 and mesh adjustment via using the Laplace method, as was described for a channel with indented wall case. The above procedure is repeated at the beginning of each new time step.

3. DOMAIN DISCRETIZATION

To extend our FV-based FE formulation, we need describing the volumes and elements and their relations. Figure 3 shows nine neighboring either quadrilateral or triangular elements in one part of the solution domain in a specific time step. The solid lines define elements, the dashed lines define their medians, and the solid circles represent the cell centers or element vertices. The quadrilateral and triangular elements are, respectively, divided into four and three parts using their medians. The proper assemblage of the sub-control volumes (SCVs) distributed around each solid circle creates a cell or a control volume, see the shaded area in Figure 3. The created control volume in Figure 3 consists of five SCVs numbered from SCV1 to SCV5. Using the Green theorem, the volume integral over a cell can be reduced to an assemblage of surface integrals over the faces of that cell. As is seen in this figure, the boundary of the chosen control volume consists of 10

DOI: 10.1002/fld

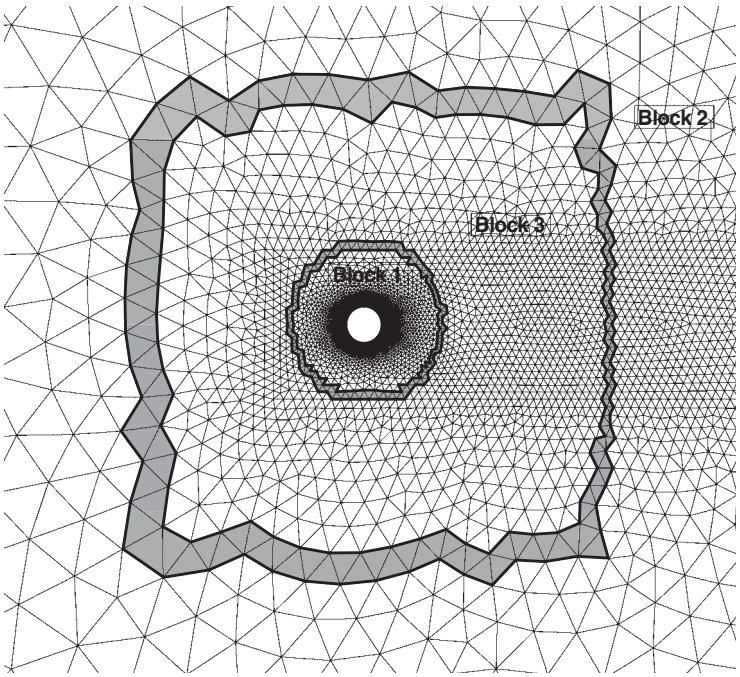

Figure 2. The solution domain over a transversely oscillating cylinder is divided into three mesh blocks of which block 3 performs mesh deformation.

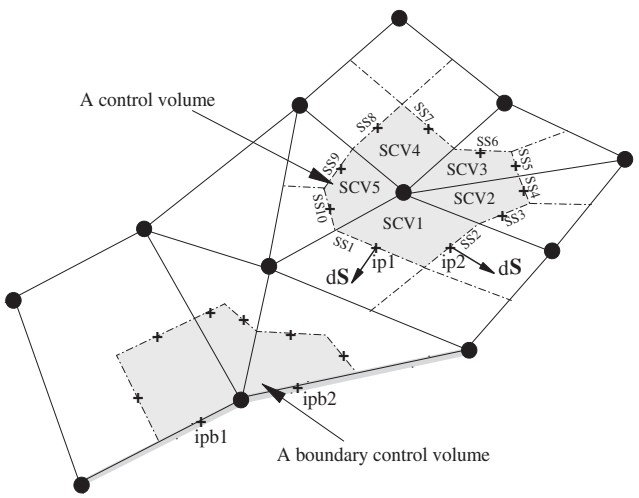

Figure 3. The illustration of a complete cell and an incomplete boundary cell and the constructed cell faces around them.

DOI: 10.1002/fld

sub-surfaces, i.e. SS1 to SS10. All the fluxes are approximated at the center of each sub-surface, which is shown by a plus symbol and is called integration point ip. For the sake of simplicity, only ip1 and ip2 are shown in this figure. The figure also shows the location of two integration points located on the boundary cell faces, i.e. ipb1 and ipb2. As is seen, the boundary integration points are located at the edges of boundary elements. In the following section, we use uppercase letters such as P, U, V, and Θ to refer to the magnitudes at FE vertices or cell centers and lowercase letters such as p, u, v, and θ to denote the magnitudes at the cell faces or integration points.

4. THE GOVERNING EQUATIONS

The Lagrangian–Eulerian space is a reference space. If the velocities of the mesh nodes and the fluid particles are the same, the Lagrangian–Eulerian space becomes a Lagrangian space and if the velocities of the mesh nodes are zero, it becomes an Eulerian space. The time integral forms of the 2D governing equations in the Lagrangian–Eulerian space, for an arbitrary moving cell with a volume of $\mathscr{V}(t)$ and a cell-face area of $S(t)$, are given by

$$\frac{\mathrm{d}}{\mathrm{d}t}\iiint_{\mathscr{V}(t)}\rho\,\mathrm{d}\mathscr{V}+\iint_{S(t)}\rho(\mathbf{V}-\mathbf{V}')\cdot\mathrm{d}\mathbf{S}=0 \tag{2a}$$

$$\frac{\mathrm{d}}{\mathrm{d}t}\iiint_{\mathscr{V}(t)}\rho\mathbf{V}\,\mathrm{d}\mathscr{V}+\iint_{S(t)}\rho\mathbf{V}(\mathbf{V}-\mathbf{V}')\cdot\mathrm{d}\mathbf{S}=\iint_{S(t)}\sigma\hat{\mathbf{n}}\,\mathrm{d}S \tag{2b}$$

$$\frac{\mathrm{d}}{\mathrm{d}t}\iiint_{\mathscr{V}(t)}\rho\theta\,\mathrm{d}\mathscr{V}+\iint_{S(t)}\rho\theta(\mathbf{V}-\mathbf{V}')\cdot\mathrm{d}\mathbf{S}=\iint_{S(t)}\mathbf{q}\cdot\mathrm{d}\mathbf{S} \tag{2c}$$

where $\mathbf{V}=u\hat{\mathbf{i}}+v\hat{\mathbf{j}}$ is the flow velocity vector, $\mathbf{V}'=u'\hat{\mathbf{i}}+v'\hat{\mathbf{j}}$ is the cell-face velocity vector, $\hat{\mathbf{n}}=(n_{\mathbf{x}})\hat{\mathbf{i}}+(n_{\mathbf{y}})\hat{\mathbf{j}}$ is a unit vector normal to the cell face, and $\mathrm{d}\mathbf{S}=(\mathrm{d}S_{\mathbf{x}})\hat{\mathbf{i}}+(\mathrm{d}S_{\mathbf{y}})\hat{\mathbf{j}}$ is an outward normal vector to the cell face with a total magnitude of $\mathrm{d}S=[(\mathrm{d}S_{\mathbf{x}})^2+(\mathrm{d}S_{\mathbf{y}})^2]^{1/2}$, $\mathrm{d}S_{\mathbf{x}}=\Delta y$, and $\mathrm{d}S_{\mathbf{y}}=-\Delta x$. Additionally, ρ and θ represent density and temperature variables. The surface forces appear in the rhs of Equation (2b). The total stress tensor σ includes the hydrostatic pressure p and stress tensor terms τ. It is given by

$$\sigma_{ij}=-p\delta_{ij}+\tau_{ij} \tag{3}$$

The stress tensor τ and the conductive heat flux vector $\mathbf{q}=q_x\hat{\mathbf{i}}+q_y\hat{\mathbf{j}}$ for the incompressible Newtonian fluid flow are derived from

$$\tau_{ij}=\mu\left(\frac{\partial u_i}{\partial x_j}+\frac{\partial u_j}{\partial x_i}\right),\quad \mathbf{q}=\left(-k\frac{\partial\theta}{\partial x}\right)\hat{\mathbf{i}}+\left(-k\frac{\partial\theta}{\partial y}\right)\hat{\mathbf{j}} \tag{4}$$

where μ and k are the fluid viscosity and conductivity coefficients, respectively. To obtain the non-dimensional form of the governing equations, we define

$$\begin{aligned} &x^*=\frac{x}{D},\quad y^*=\frac{y}{D},\quad u^*=\frac{u}{V_\infty},\quad v^*=\frac{v}{V_\infty},\quad \rho^*=\frac{\rho}{\rho_\infty}\\ &p^*=\frac{p-p_\infty}{\rho_\infty V_\infty^2},\quad t^*=\frac{t}{D/V_\infty},\quad \theta^*=\frac{\theta-\theta_\infty}{\theta_{\mathrm{w}}-\theta_\infty} \end{aligned} \tag{5}$$

DOI: 10.1002/fld

where the subscript ∞ denotes the free stream or reference conditions. In our incompressible formulations, $\rho=\rho_\infty=1$. The subscript w denotes the magnitude at the wall. D presents a characteristic length scale such as the channel height or the cylinder diameter. Introducing the non-dimensional parameters into Equations (2) and dropping the symbol *, the non-dimensional form of the governing equations is condensed to

$$\frac{\mathrm{d}}{\mathrm{d}t}\iiint_{\mathscr{V}(t)}\psi\,\mathrm{d}\mathscr{V}+\iint_{S(t)}(\mathscr{F}\,\mathrm{d}S_x+\mathscr{G}\,\mathrm{d}S_y)-\iint_{S(t)}(\mathscr{F}'\,\mathrm{d}S_x+\mathscr{G}'\,\mathrm{d}S_y)$$
$$=\iint_{S(t)}(\mathscr{R}\,\mathrm{d}S_x+\mathscr{T}\,\mathrm{d}S_y) \tag{6}$$

This equation represents the continuity, momentums, and energy conservation laws. In the above equation, $\psi=[\rho, f, g, \theta]^{\mathrm{T}}$, where $f=\rho u$ and $g=\rho v$ are the momentum components in the x and y directions, respectively. The convection flux vectors $\mathscr{F}$, $\mathscr{G}$, $\mathscr{F}'$, and $\mathscr{G}'$ and the diffusion flux vectors $\mathscr{R}$ and $\mathscr{T}$ are given by

$$\mathscr{F}=[f, uf+p, ug, u\theta]^{\mathrm{T}},\quad \mathscr{G}=[g, vf, vg+p, v\theta]^{\mathrm{T}} \tag{7a}$$

$$\mathscr{F}'=[f', u'f, u'g, u'\theta]^{\mathrm{T}},\quad \mathscr{G}'=[g', v'f, v'g, v'\theta]^{\mathrm{T}} \tag{7b}$$

$$\mathscr{R}=[0, \tau_{11}, \tau_{21}, q_x]^{\mathrm{T}},\quad \mathscr{T}=[0, \tau_{12}, \tau_{22}, q_y]^{\mathrm{T}} \tag{7c}$$

where $f'=\rho u'$ and $g'=\rho v'$. The non-dimensional stress tensor and the conduction heat flux components are calculated from [20]

$$\begin{aligned}&\tau_{11}=\frac{2}{\mathrm{Re}}\frac{\partial f}{\partial x},\quad \tau_{22}=\frac{2}{\mathrm{Re}}\frac{\partial g}{\partial y},\quad \tau_{12}=\tau_{21}=\frac{1}{\mathrm{Re}}\left(\frac{\partial f}{\partial y}+\frac{\partial g}{\partial x}\right)\\ &q_x=-\frac{1}{\mathrm{Re}\,\mathrm{Pr}}\frac{\partial\theta}{\partial x},\quad q_y=-\frac{1}{\mathrm{Re}\,\mathrm{Pr}}\frac{\partial\theta}{\partial y}\end{aligned} \tag{8}$$

where $\mathrm{Re}=\rho V_\infty D/\mu$ and Pr denote the Reynolds and Prandtl numbers, respectively.

5. COMPUTATIONAL MODELING

The integration of Equation (6) over the cell shown in Figure 3 can be approximated by

$$\frac{\mathrm{d}}{\mathrm{d}t}\left\{\sum_m[\psi]_m\mathscr{V}\right\}+\sum_m[\mathscr{F}(\Delta S_x)+\mathscr{G}(\Delta S_y)]_m$$
$$-\sum_m[\mathscr{F}'(\Delta S_x)+\mathscr{G}'(\Delta S_y)]_m=\sum_m[\mathscr{R}(\Delta S_x)+\mathscr{T}(\Delta S_y)]_m \tag{9}$$

where $\mathscr{V}$ is the cell volume and m counts the 10 sub-surfaces from SS1 to SS10 located on the cell face. The treatment of terms in the brackets appearing in Equation (9) is described one by one now. We start from the unsteady term. Writing Taylor-series expansions for $\mathscr{V}^{n-1}$ and $\mathscr{V}^n$ expanding about time $n+1$ and attempting to solve for $(\partial\mathscr{V}/\partial t)^{n+1}$ from the resulting equations in such a way as to obtain a truncation error of $O(\Delta t)^2$, one can reach the second-order time accurate discretization for this term. Considering the volume of the cell as a function of time,

DOI: 10.1002/fld

the discretizations of this term using either the first-order or the second-order approximations eventually yield [21]

$$\text{First order:} \quad \frac{\mathrm{d}(\psi\mathscr{V})}{\mathrm{d}t} = \frac{(\psi\mathscr{V})^{n+1} - (\psi\mathscr{V})^{n}}{\Delta t} \tag{10a}$$

$$\text{Second order:} \quad \frac{\mathrm{d}(\psi\mathscr{V})}{\mathrm{d}t} = \frac{3(\psi\mathscr{V})^{n+1} - 4(\psi\mathscr{V})^{n} + (\psi\mathscr{V})^{n-1}}{2\Delta t} \tag{10b}$$

where Δt is the time step and n counts the time advancement. The details of the second-order derivations can be found in Reference [21].

The diffusion terms in the rhs of Equation (9) can be approximated using the gradients of FE shape functions. For example, the diffusion terms in the x-momentum equation at the sub-surface m are discretized to

$$\begin{aligned}[\mathscr{R}(\Delta S_x) + \mathscr{T}(\Delta S_y)]_m &= \frac{1}{\mathrm{Re}}\left[\left(2\frac{\partial f}{\partial x}\right)\Delta S_x + \left(\frac{\partial f}{\partial y} + \frac{\partial g}{\partial x}\right)\Delta S_y\right]_m \\ &= \frac{1}{\mathrm{Re}} \sum_{j=1}^{3 \text{ or } 4} \left(2\frac{\partial N_j}{\partial x}\Delta S_x + \frac{\partial N_j}{\partial y}\Delta S_y\right)_m F_j \\ &\quad + \frac{1}{\mathrm{Re}} \sum_{j=1}^{3 \text{ or } 4} \left(\frac{\partial N_j}{\partial x}\Delta S_y\right)_m G_j \end{aligned} \tag{11}$$

where N is the FE shape function and j counts the number of nodes in the element, where the chosen integration point is located. Depending on the shape of an element, the number of nodes is 3 or 4. As is seen in Equation (11), $F = \rho U$ is a dependent variable in our algorithm. In fact, we have chosen P, $F = \rho U$, $G = \rho V$, and Θ as the major dependent variables in our algorithm, as were chosen by References [14, 15, 22]. The diffusion terms in the y-momentum equation are also treated similar to the treatment given in Equation (11).

The second and third summations in the lhs of Equation (9) present the convection terms, which are the most sensible terms in view of their physics in the fluid dynamics, and especially in the flow fields with a high deformable mesh. The third summation presents mesh node velocities. The approximation of this term is fulfilled via implementing the GCL, i.e. via the surface and volume conservation laws. The surface conservation law states that the FVs must remain closed during the mesh movement. The volume conservation law is more important than the surface conservation law and it needs to be satisfied either explicitly or implicitly during a mesh movement. Essentially, the volume conservation law states that the mesh node movement must not affect the conservation laws if the domain boundaries do not move. The flow governing equations are used to obtain the volume conservation laws in solving the flow field with fixed boundaries. First, we consider a fluid flow having a constant density and a zero velocity. The mass conservation law yields

$$\sum_{m} [u'(\Delta S_x) + v'(\Delta S_y)]_m = \frac{\mathrm{d}\mathscr{V}}{\mathrm{d}t} \tag{12}$$

DOI: 10.1002/fld

The time variation of the volume can be approximated using either the first-order or the second-order accurate finite differences. The use of the first-order scheme yields

$$\frac{\mathrm{d}\mathscr{V}}{\mathrm{d}t} \cong \frac{\mathscr{V}^{n+1}-\mathscr{V}^{n}}{\Delta t} = \frac{\Delta\mathscr{V}^{n+1}}{\Delta t} \tag{13}$$

while the use of the second-order scheme results in [21]

$$\frac{\mathrm{d}V}{\mathrm{d}t} \cong \frac{(3/2)\mathscr{V}^{n+1}-2\mathscr{V}^{n}+(1/2)\mathscr{V}^{n-1}}{\Delta t} \tag{14}$$

Contrary to the first-order scheme, the second-order scheme needs an additional procedure as follows:

$$\begin{aligned}\frac{\mathrm{d}\mathscr{V}}{\mathrm{d}t} &\cong \frac{(3/2)(\mathscr{V}^{n+1}-\mathscr{V}^{n})-2(\mathscr{V}^{n}-\mathscr{V}^{n})+(1/2)(\mathscr{V}^{n-1}-\mathscr{V}^{n})}{\Delta t}\\ &= \frac{(3/2)(\Delta\mathscr{V}^{n+1})-(1/2)(\Delta\mathscr{V}^{n})}{\Delta t}\end{aligned} \tag{15}$$

where $\Delta\mathscr{V}^{n+1}=\mathscr{V}^{n+1}-\mathscr{V}^{n}$ and $\Delta\mathscr{V}^{n}=\mathscr{V}^{n}-\mathscr{V}^{n-1}$. If the surface movement causes a cell enlargement, the magnitude of $\mathrm{d}\mathscr{V}/\mathrm{d}t$ will be positive and vice versa. Considering 2D formulations, a volume is an area per unit depth. In practice, the change of the cell area is equal to the summation of sub-areas swept by the cell faces during their movements. Considering this point, Equation (15) can be generalized to

$$\frac{\mathrm{d}\mathscr{V}}{\mathrm{d}t} = \sum_{m}\frac{\partial V_m}{\partial t} = \sum_{m}\frac{(3/2)(\Delta\mathscr{V}_m^{n+1})-(1/2)(\Delta\mathscr{V}_m^{n})}{\Delta t} \tag{16}$$

The cell volume changes $\Delta\mathscr{V}_m^{n+1}$ and $\Delta\mathscr{V}_m^{n}$ for an SCV located in a triangle element are shown in Figure 4. The subscript m denotes SS1 and SS2 in this SCV. In this figure, nodes 1 and 2 are fixed, while node 3 is moving. If the positions of node 3 are known at three $n-1$, n, and $n+1$ time steps, the volume changes, i.e. $\Delta\mathscr{V}_m^{n+1}$ and $\Delta\mathscr{V}_m^{n}$, can be readily calculated considering the areas swept by the SS1 and SS2 faces on the constructed control volume around node 1. In reality, they are known.

This strategy can be followed for all SS's around node 1. Using this knowledge, we can approximate the lhs of Equation (12) as follows:

$$[u'(\Delta S_x)+v'(\Delta S_y)]_m = \frac{\mathrm{d}\mathscr{V}_m}{\mathrm{d}t} = \Omega_m \tag{17}$$

Therefore, the third summation on the lhs of Equation (9) can be expressed as $\bar{f}_{\mathrm{ip}}\Omega_{\mathrm{ip}}$, $\bar{g}_{\mathrm{ip}}\Omega_{\mathrm{ip}}$, and $\bar{\theta}_{\mathrm{ip}}\Omega_{\mathrm{ip}}$ in the x-momentum, y-momentum, and energy equations, respectively. Back to Figures 3 and 4, m's are the same as ip's. The bar over f, g, and θ indicates that these variables are approximated from either the preceding iteration or time step.

As is understood from Equations (7) and (9), the convection terms are non-linear with respect to our chosen dependent variables (F, G, P, and Θ) and they must be linearized properly. We may use a simple way to linearize them to

$$\mathscr{F}=[\hat{f},\bar{\hat{u}}f+p,\bar{\hat{u}}g,\bar{\hat{u}}\theta], \quad \mathscr{G}=[\hat{g},\bar{\hat{v}}f,\bar{\hat{v}}g+p,\bar{\hat{v}}\theta] \tag{18}$$

DOI: 10.1002/fld

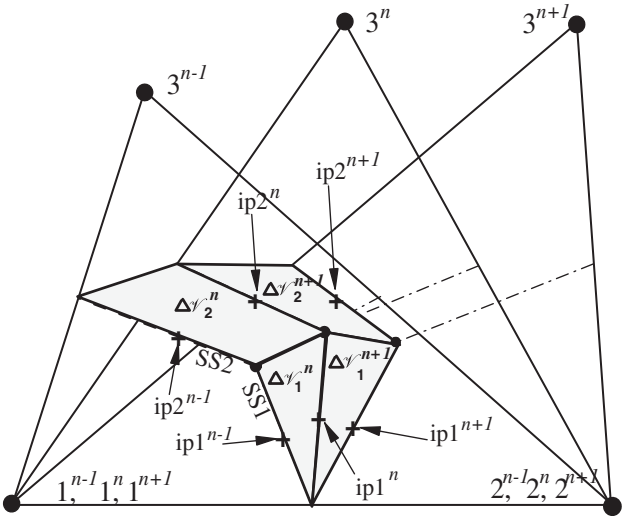

Figure 4. The areas swept by SS1 and SS2 cell faces.

The hats over the above variables indicate that there are two types of convecting and convected variables in the formulation [14, 15, 17]. These variables are explained shortly. Mathematically, all the elements in Equation (18) can be approximated at the integration points. However, we must be very careful in choosing the type of approximation. Basically, the terms appearing in the non-linear convection terms must be treated physically rather than mathematically. If we write the convection terms in the direction of the streamlines, two streamwise upwinding statements can be obtained. They approximate f and g at the integration points. For instance, the unsteady x-momentum equation can be expressed in the streamwise direction as

$$V_{\text{tot}}\frac{\partial f}{\partial s}+\frac{\partial p}{\partial x}=-\frac{\partial \bar{f}}{\partial t}+\left(\frac{\partial \tau_{11}}{\partial x}+\frac{\partial \tau_{12}}{\partial y}+\Gamma\right) \tag{19}$$

where $V_{\text{tot}}=\sqrt{\bar{u}^2+\bar{v}^2}$ and $\Gamma=u'\partial f/\partial x+v'\partial f/\partial y$. The terms in the parentheses are assumed to be known. In other words, they are calculated using the magnitudes of the variables from the preceding time step or iteration. The unsteady term can be discretized using either the first-order or the second-order approaches as follows [21]:

$$\frac{\partial \bar{f}}{\partial t}\cong\frac{\bar{f}^{n+1}-\bar{f}^{n}}{\Delta t} \tag{20a}$$

$$\frac{\partial \bar{f}}{\partial t}\cong\frac{3\bar{f}^{n+1}-4\bar{f}^{n}+\bar{f}^{n-1}}{2\Delta t} \tag{20b}$$

in which $\bar{f}^{n+1}$ is approximated from the previous iteration and the other parts are properly obtained from the past time steps.

DOI: 10.1002/fld

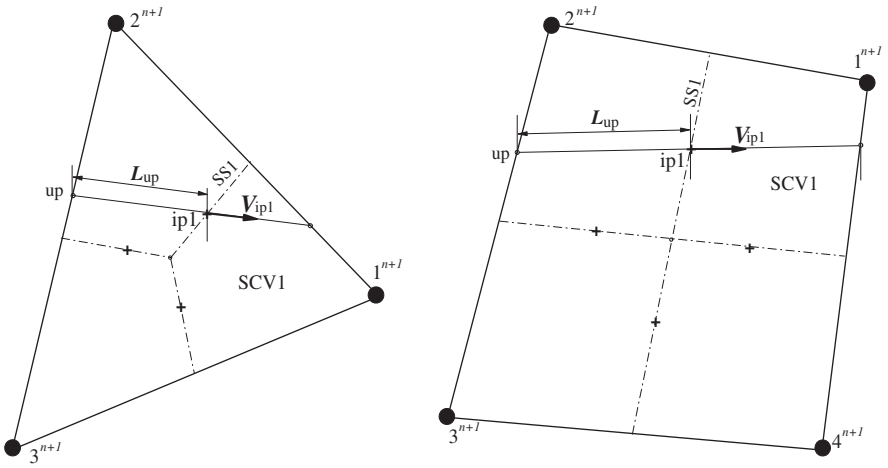

Figure 5. Triangular and quadrilateral element nomenclatures and the streamwise velocity upwinding strategy within them.

The convection term in Equation (19) is discretized using an upwind strategy in the streamline direction. In other words, $\partial f/\partial s$ is discretized using an upwind strategy. It yields

$$\left[V_{\text{tot}}\frac{\partial f}{\partial s}\right]_{\text{ip}} = \left[V_{\text{tot}}\frac{\partial f}{\partial s}\right]_m \cong (V_{\text{tot}})_m \frac{f_m - (f_{\text{up}})_m}{(L_{\text{up}})_m} \tag{21}$$

Referring to Figure 5, the subscript 'up' indicates the upwind point, where the streamline passing through ip1 crosses the edge of the same element, which includes ip1. In this figure, the upwind lengths L_{up} are shown for the integration point 1 (ip1) in both triangular and quadrilateral elements. We can further use FE shape functions to calculate f_{up} as follows:

$$f_{\text{up}} = \sum_{j=1}^{3 \text{ or } 4} (N_j)_{\text{up}} F_j \tag{22}$$

The pressure gradient term in Equation (19) is treated using the gradients of the FE shape functions. For example, this consideration for $\partial p/\partial x$ term yields

$$\left(\frac{\partial p}{\partial x}\right)_m = \sum_{j=1}^{3 \text{ or } 4} \left(\frac{\partial N_j}{\partial x}\right)_m P_j \tag{23}$$

Eventually, considering a mass-lumped approach and using the shape functions and their gradients, the diffusion terms and node velocity source terms are approximated by

$$\left(\frac{\partial \tau_{11}}{\partial x} + \frac{\partial \tau_{12}}{\partial y} + \Gamma\right) = \frac{1}{\mathscr{V}} \sum_m (\bar{\tau}_{11}\Delta S_x + \bar{\tau}_{12}\Delta S_y + \bar{f}\Omega)_m \tag{24}$$

where the bar over variables indicates that they are explicitly approximated at the mid-cell faces using the known magnitude of variables from the preceding steps or iterations.

DOI: 10.1002/fld

At this stage, the modeling of all terms in Equation (19) is complete. The substitutions of Equations (20)–(24) in Equation (19) and its rearrangement yield a new statement for f at the mth integration point. The statement can be condensed to

$$f_m = \sum_{j=1}^{3 \text{ or } 4} [\alpha_{mj}^{ff} F_j + \alpha_{mj}^{fp} P_j] + \gamma_m^f \tag{25}$$

where α_{mj}^{ff} and α_{mj}^{fp} are two matrices having 4×4 sizes in the case of the quadrilateral elements and 3×3 sizes in the case of the triangular elements. In fact, Equation (25) shows the direct impacts of F and P fields in approximating f_m or f_{ip}. In other words, it shows the influence of pressure and momentum component values at the element vertices on the value of f at the cell face. The γ_m^f vector involves all the terms with known magnitudes and has a 4×1 size for the quadrilateral elements and a 3×1 size for the triangular elements. The superscripts over α from left to right denote to which equation and which coefficient of that equation it is multiplied. Similar to Equation (25), an expression can be derived for g at an arbitrary integration point starting from the y-momentum equation. It eventually yields

$$g_m = \sum_{j=1}^{3 \text{ or } 4} (\alpha_{mj}^{gg} G_j + \alpha_{mj}^{gp} P_j) + \gamma_m^g \tag{26}$$

The derived convection fluxes, f_m and g_m, in Equations (25) and (26) show that the magnitudes at an arbitrary integration point are related to the magnitudes at its neighboring nodes and they can be readily substituted in the convection terms of the momentum equations. By these substitutions, the discretized equations are totally expressed in terms of the variables defined at the nodal points or at the element vertices.

As the last stage, it remains to remove the pressure-checkerboard problem, which may arise in our collocated-grid FVE method. In order to avoid the pressure-checkerboard problem, we employ a combination of Rhie and Chow [16] interpolation and the concept of physical upwinding scheme [17]. This strategy needs two new momentum integration point expressions to be created. They should be different from those presented in Equations (25) and (26). Therefore, we use hats over them, i.e. $\hat{f}$ and $\hat{g}$, to distinguish them from the previous ones. These new momentum components will be expressed in terms of nodal values and they are substituted only in the continuity equation, see Equation (18). We apply the idea in References [15, 18, 19] and extend it properly to our moving mesh FVE-ALE approach. In order to derive $\hat{f}$, the x-momentum equation is rewritten as

$$V_{\text{tot}} \frac{\partial \hat{f}}{\partial s} + \frac{\partial p}{\partial x} - f\left(\frac{\partial f}{\partial x} + \frac{\partial g}{\partial y}\right) = -\frac{\partial f}{\partial t} + \left(\frac{\partial \tau_{11}}{\partial x} + \frac{\partial \tau_{12}}{\partial y} + \Gamma\right) \tag{27}$$

With the exception of the terms within the parentheses on the lhs, the remaining terms are discretized similar to those in Equation (19). The terms inside the lhs parentheses are discretized using the gradients of FE shape functions; see Equation (23). After suitable discretizations of all the terms, they are substituted in Equation (27). We finally obtain

$$\hat{f}_m = \sum_{j=1}^{3 \text{ or } 4} (\alpha_{mj}^{\hat{f}f} F_j + \alpha_{mj}^{\hat{f}g} G_j + \alpha_{mj}^{\hat{f}p} P_j) + \gamma_m^{\hat{f}} \tag{28}$$

DOI: 10.1002/fld

Once more, this equation includes the direct impacts of F, G, and P fields in calculating $\hat{f}_m$ or $\hat{f}_{\text{ip}}$. Similarly, we derive an equation for $\hat{g}$ starting from the y-momentum equation. It eventually yields

$$\hat{g}_m = \sum_{j=1}^{3 \text{ or } 4} (\alpha_{mj}^{\hat{g}f} F_j + \alpha_{mj}^{\hat{g}g} G_j + \alpha_{mj}^{\hat{g}p} P_j) + \gamma_m^{\hat{g}} \tag{29}$$

The size of matrices and the definition of superscripts in Equations (28) and (29) are the same as those described in Equations (25) and (26). It should be noted that (f and g) and ($\hat{f}$ and $\hat{g}$) are collocated. By substituting the momentum components given in Equations (28) and (29) in the continuity equation, the pressure-checkerboard problem is fully suppressed [14, 15, 17]. The substitutions will cause direct presence of pressure in the mass conservation equation and this removes the need for additional auxiliary equations, e.g. the Poisson pressure equation, to couple the pressure and velocity in our collocated-grid approach.

As is shown in Figure 3, we utilize two boundary integration points of ipb1 and ipb2 located at the boundary elements to close the FVs located on the boundaries. At these integration points, the magnitudes of flow field variables are either known or unknown. For example, the velocities are known at the inlet, the pressure is known at the outlet, and the velocities are unknown at the outlet and need to be calculated. On the walls, the velocities of flow particles are equal to the velocity of boundaries; therefore, the velocities of integration points located on the boundaries are known. If the magnitude of a variable at one boundary is not known, the conservative forms of the governing equations are closed at those boundary faces. Darbandi and Vakilipour [23] have shown that the current method would be very robust, even specifying the outlet boundary condition at an improper section far from the chosen outflow and very close to the inflow section.

At this stage, the modelings of the unsteady, diffusion, and convection terms in Equation (9) are completed. The substitutions of these terms in Equation (9) result in four conservative equations for each control volume. Alternatively, the assemblages of all the element stiffness matrices into the global stiffness matrix produce a linear system of algebraic equations. The set of equations for the continuity and two momentum equations can be cast into

$$\begin{aligned} c_{ij}^{pf} F_j + c_{ij}^{pg} G_j + c_{ij}^{pp} P_j &= d_i^p \\ c_{ij}^{ff} F_j + c_{ij}^{fg} G_j + c_{ij}^{fp} P_j &= d_i^f \\ c_{ij}^{gf} F_j + c_{ij}^{gg} G_j + c_{ij}^{gp} P_j &= d_i^g \end{aligned} \tag{30}$$

where i and j count the global node numbers and c identifies the elements of the global stiffness matrix. The first superscript of c represents the type of equation, i.e. p for the continuity, f for the x-momentum, and g for the y-momentum. The second superscript represents the name of unknown, which is multiplied by c.

In incompressible flow calculations, the energy equation is decoupled from the mass and momentum equations. Therefore, after calculating the velocity and pressure fields, the temperature field can be solved separately. Up to here, the modelings of various terms in the energy equation have been described indirectly via treating the continuity and momentum equations. After the substitutions of the equivalent models in Equation (9) and the assemblage of all the element

DOI: 10.1002/fld

stiffness matrices in the global matrix, a linear system of algebraic equations is generated for the temperature field as follows:

$$c_{ij}^{\theta\theta}\Theta_j = d_i^{\theta} \tag{31}$$

The sets of linear algebraic equations presented in Equations (30) and (31) are highly sparse and need to be solved using suitable sparse matrix solvers. To solve the resulting system of algebraic equations more robustly, we employ preconditioners. Darbandi *et al.* [24, 25] have tried different sparse solver systems. They found that the best iterative solver would be GMRES and the best precondition would be ILU. We have used these methods to solve our linear systems of equations more efficiently.

6. RESULTS AND DISCUSSION

Before examining the results of our FVE-ALE formulations, we would like to evaluate the accuracy of our extended physical-influence scheme (PIS) utilized to approximate the convection fluxes at the cell faces, see Equations (25)–(26) and (28)–(29). As is known, the use of the first-order upwinding generates excessive numerical diffusion, specially in cases where the flow is not aligned with the grid lines. Since the extended physical-influence upwind scheme is a contribution of this study, there might be a question whether this scheme creates crosswind diffusion. In the literature, the crosswind diffusion of the schemes such as upwind, central, etc. is examined via treating the classical convection–diffusion test. However, since our PIS expression involves the pressure gradients, the treatment of the classical convection–diffusion test cannot reveal its capabilities. Therefore, we examine our PIS via solving a fluid flow problem, where the grid lines are generally not aligned with the flow. The test case is the fluid flow through a channel with an aspect ratio of 20×1 and a Reynolds number of 10 000. In this Reynolds number, the convection terms are dominant. The inlet boundary condition is a fully developed velocity profile and its mean value is unity. A uniform pressure is fixed at the outlet. Four different uniform grid resolutions of 40×4, 80×8, 160×16, and 320×32 are considered for the channel. Figure 6 schematically demonstrates a part of 40×4 mesh resolution close to the inlet. The figure also compares velocity profiles at the inlet (solid lines) with those at the outlet (dashed lines). It is seen that the velocity profiles at the inlet and the outlet are almost the same at all mesh resolutions, even the coarse ones. No crosswind diffusion is observed here. Indeed, the current authors had previously shown that the PIS provides very accurate solutions on non-deformable meshes, even employing very coarse grid distributions, see References [14, 15, 18, 19].

We first test the flow around a fixed circular cylinder placed in a free stream flow to verify the accuracy of the present method in solving the unsteady flows with a zero mesh velocity. There are many numerical and experimental studies in the literature, which solve this test case in detail. These references generally study and report the generated vortex shedding and its resulting frequency, the lift and drag coefficients, base-pressure coefficient, separation points, heat transfer rate, and so on. The cylinder has a unit diameter and the spatial sizes are non-dimensionalized with respect to it. Specifying a unit diameter for the cylinder, the distance between the top and bottom boundaries is 100 units, and the distances from the center of the cylinder to the inflow and outflow sections are 50 and 100 units, respectively. These distances are chosen following the experiences of [26]. Our experience also showed that a computational domain with a larger size would slightly improve our lift and drag coefficients and Strouhal and Nusselt numbers. The top and bottom boundaries

DOI: 10.1002/fld

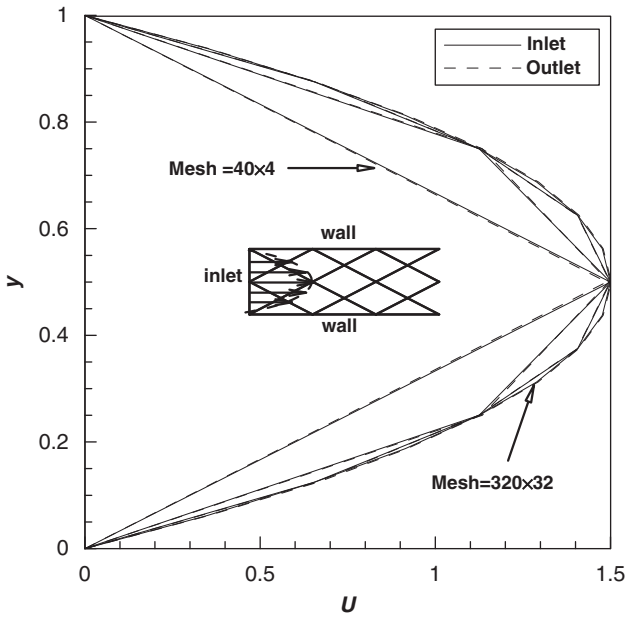

Figure 6. Demonstration of the grid distribution nearby the inlet of a channel and comparison of the velocity profiles at its inlet and outlet sections, Re = 10 000.

are treated as free stream. The longitudinal velocities at the inlet and free stream boundaries are all unity. The transversal velocity is zero at the inlet. The non-dimensional temperature is zero at the inlet and top and bottom boundaries. The temperature is unity at the cylinder face. A unit pressure is fixed at the outflow. As the initial conditions, the velocity, pressure, and temperature are chosen to be unity. The chosen Reynolds numbers are 100, 150, and 200.

We use a hybrid mesh to discretize the computational domain around the cylinder. As was described in Sections 2 and 3, it involves structured quadrilateral elements close to the cylinder and unstructured elements with either triangular or quadrilateral shapes in the rest of the domain. Figure 7 shows two pictures of the mesh nearby and far from the cylinder. We distribute three different mesh distributions in the domain. They include 1818, 3823, and 7688 nodes. They are called coarse, moderate, and fine meshes, respectively. There are 40, 80, and 160 nodes around the cylinder and the distances of the closest node from the wall are 0.02, 0.01, and 0.005, respectively. These distances are less than the viscous length scale at the front stagnation point in all Reynolds numbers [27].

Table I reports the impacts of mesh and time step sizes in the solutions when Re = 200. The table presents the lift and drag coefficients as well as the Strouhal and Nusselt numbers. The Strouhal number and the Nusselt number represent the non-dimensional frequency f_0 of the vortex shedding and the non-dimensional heat rate q from the cylinder. They are defined as $\mathrm{St} = (f_0 D)/V_\infty$ and $\mathrm{Nu} = (qD)/[k(\theta_\mathrm{w} - \theta_\infty)]$. In this table, the bar over a parameter denotes its mean-time value and the prime denotes its root-mean-squared or rms value. Three time steps are examined and both the first-order and the second-order time accuracies are investigated. Time refinement study is carried out using time steps of 0.1, 0.05, and 0.01, which result in Courant numbers $(V_\infty \Delta t/\Delta x)$

DOI: 10.1002/fld

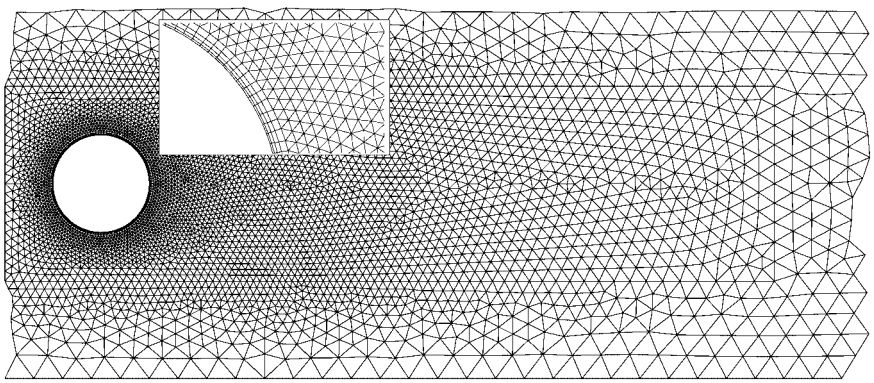

Figure 7. Two views of the mesh distribution around and nearby the cylinder, test 1.

Table I. Time step and mesh refinement studies for a fixed cylinder in a free stream with Re = 200, test 1.

Time accuracy →		First order					Second order				
No. of nodes ↓	$\Delta t \downarrow$	C_l'	C_d'	$\overline{C_d}$	St	$\overline{\mathrm{Nu}}$	C_l'	C_d'	$\overline{C_d}$	St	$\overline{\mathrm{Nu}}$
1818	0.10	0.411	0.024	1.202	0.149	7.25	0.546	0.037	1.325	0.166	7.38
	0.05	0.482	0.031	1.256	0.158	7.32	0.548	0.037	1.324	0.168	7.38
	0.01	0.523	0.035	1.299	0.162	7.36	0.548	0.037	1.322	0.169	7.38
3823	0.10	0.330	0.017	1.201	0.175	7.18	0.482	0.032	1.325	0.192	7.34
	0.05	0.401	0.024	1.255	0.182	7.25	0.484	0.032	1.324	0.192	7.34
	0.01	0.448	0.028	1.293	0.188	7.30	0.483	0.032	1.321	0.192	7.34
7688	0.10	0.333	0.017	1.207	0.175	7.20	0.493	0.033	1.337	0.192	7.37
	0.05	0.406	0.024	1.263	0.183	7.28	0.494	0.033	1.334	0.192	7.37
	0.01	0.457	0.029	1.304	0.189	7.33	0.494	0.033	1.331	0.192	7.37

ranging from 20 to 2.5. As is seen in this table, the magnitudes of the first-order scheme are more scattered than those of the second-order scheme. All the magnitudes in the second-order scheme, and specially using the fine and moderate mesh resolutions, are nearly the same despite using different time steps. In the case of using the second-order scheme, the values of some parameters in the case of coarse mesh are slightly far from those of the moderate and fine ones. A decrease in the time step of the first-order scheme leads to results close to the results of the second-order scheme at all mesh resolutions, even the coarse one.

The time variations of the lift and drag coefficients are shown in Figure 8 using a fine mesh and the first-order time accurate scheme at Re = 200. Time is non-dimensionalized using $T^* = tV_\infty/D$. At $T^* > 70$, the lift and drag diagrams remain harmonic. Decreasing the time step from 0.1 to 0.05 at $T^* = 200$, the oscillations of the lift and drag coefficients change abruptly. In addition, a similar behavior is observed when the time step decreases from 0.05 to 0.01 at $T^* = 400$. Figure 9 plots the vorticity contours at Re = 200. As is observed, two lines of vorticities are generated behind the cylinder and they are shed into the flow field and exit from the outlet. The dashed lines denote negative magnitudes and the solid lines have positive magnitudes. The Strouhal number at this Reynolds number is 0.192.

DOI: 10.1002/fld

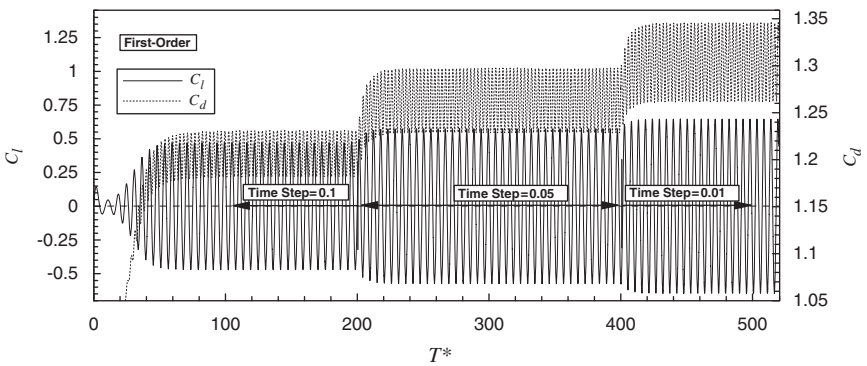

Figure 8. Time variation of the lift and drag coefficients at Re = 200, test 1.

Figure 9. The vortex shedding captured behind the cylinder at Re = 200, test 1.

Table II compares the drag, lift, and base-pressure coefficients as well as the Strouhal number with those of other investigators. Williamson and Roshko [32] and Norberg [33] provide the experimental data. Norberg [31] collected the 2D simulation data for $\mathrm{Re} \leqslant 200$ and suggested that $C_l' = \sqrt{\varepsilon/30 + \varepsilon^2/90}$, where $\varepsilon = (\mathrm{Re} - \mathrm{Re}_c)/\mathrm{Re}_c$ and $\mathrm{Re}_c = 47$. Posdziech and Grundmann [26], Henderson [28], Lang [29], and De Sampaio *et al.* [30] present the numerical solutions. Among the numerical solutions, the results of Posdziech and Grundmann [26] are more update. They used a spectral FE method and investigated the impact of computational domain sizes on the solution. Their computational time step has been 0.005, which is very small compared with ours, which are 0.1, 0.05, and 0.01. We have presented the results of the finest mesh and the smallest time step in Table II. The results of Williamson, Norberg, Henderson, and Lang are taken from Posdziech and Grundmann [26]. As is seen, our results are the same or very close to the results of Reference [26] although our time step is chosen to be 10 times larger than that of the reference.

The averaged Nusselt $\overline{\mathrm{Nu}}$ can be calculated using Kramer's rule and curve fitting [34]. It yields

$$\overline{\mathrm{Nu}} = 0.42\mathrm{Pr}^{1/5} + 0.57\mathrm{Pr}^{1/3}\,\mathrm{Re}^{1/2} \tag{32}$$

Our average Nusselt number is about 7.55 at Pr = 0.7. However, Eckert and Drake [35] suggest

$$\overline{\mathrm{Nu}} = (0.43 + 0.5\mathrm{Re}^{1/2})\,\mathrm{Pr}^{0.38} \tag{33}$$

which results in $\overline{\mathrm{Nu}} = 6.58$. The numerical methods of Karniadakis [36] and Bouhairie and Chu [37] predict 8.30 and 6.55, respectively. Our averaged Nusselt is 7.37, which is in the mid-range of past predictions.

DOI: 10.1002/fld

Table II. The evaluation of the current solution in comparison with other numerical solutions and experimental data, test 1.

Re→		100	150	200
$\overline{C_d}$	Henderson [28]	1.350	1.333	1.341
	Lang [29]	1.338	—	1.324
	De Sampaio *et al.* [30]	—	—	1.382
	Posdziech and Grundmann [26]	1.313	1.300	1.310
	Present study	1.305	1.300	1.331
C_l'	Norberg [31]	0.228	0.355	0.476
	De Sampaio *et al.* [30]	—	—	0.499
	Present study	0.228	0.357	0.494
$-\overline{Cp_b}$	Williamson and Roshko [32]	0.709	0.854	0.834
	Norberg [33]	0.723	0.873	0.878
	Posdziech and Grundmann [26]	0.690	0.827	0.945
	Present study	0.680	0.827	0.945
St	Williamson and Roshko [32]	0.1640	0.1839	0.184
	Norberg [33]	0.1640	0.1831	—
	De Sampaio *et al.* [30]	—	—	0.195
	Posdziech and Grundmann [26]	0.1633	0.1825	0.194
	Present study	0.1587	0.1828	0.192

The second test case is a circular cylinder placed in a free stream and is transversely oscillated using a cosine movement of $y_c = A\cos(2\pi f_e)$. The amplitude of oscillation is one-fifth of the cylinder diameter ($A = 0.2D$) and its excitation frequency f_e is changed from 0.8 to 1.2 times the natural shedding frequency f_0, i.e. $0.8 \leqslant f_e/f_0 \leqslant 1.2$. The moving mesh algorithm was fully described in Section 2. The sizes of domain and cylinder, the domain boundary conditions, and the initial conditions are the same as those in test 1; however, the Reynolds number is 185. We choose the finest mesh in test 1 to study test 2. The natural shedding frequency was found to be 0.190 at this Reynolds number after careful time step and grid resolution studies. This test has also been studied by Guilmineau and Queutey [6] using an accurate boundary-transformation method and by Yang and Balaras [38] using an embedded-boundary formulation. Their finest meshes have been 240×200 and 800×640, i.e. 48 000 and 512 000 nodes, respectively. However, we used only 7688 nodes in the domain benefiting from an unstructured hybrid mesh distribution and relying on the capabilities of our PIS scheme. In other words, our finest mesh has been about 6 and 66 times coarser than those of the finest meshes in the former and latter references, respectively. The nearest nodes to the wall boundary have been $0.001D$ in the former reference and $0.005D$ in the latter reference. We chose the latter magnitude in our study as well. Furthermore, the non-dimensional time step of the former reference is 0.002, which is very small compared with 0.05 and 0.025 taken in our simulations. In other words, our smallest time step is 12.5 times greater than that in the former reference.

Figure 10 shows time variations of the lift and drag coefficients using the second-order scheme and a time step of 0.05 and $f_e/f_0 = 0.8$ and 1.2. As is observed, the lift and drag behaviors at $f_e/f_0 = 0.8$ completely differ from those obtained at $f_e/f_0 = 1.2$. This difference is due to different vortex structures at the wake region of the cylinder [6]. At this stage, we need to further evaluate the performance of our method by examining other sensitive parameters rather than the lift and drag coefficients. Figure 11 shows the skin friction and pressure coefficient distributions on the

DOI: 10.1002/fld

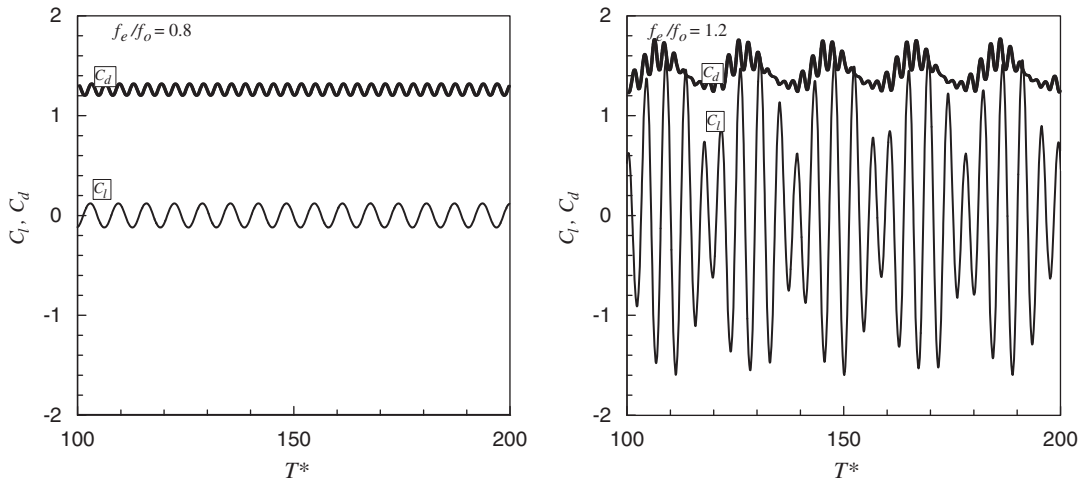

Figure 10. Lift and drag variations with time for a transversely oscillating cylinder, imposed by $f_e/f_0 = 0.8$ and 1.2, test 2.

face of the cylinder right at its extreme upper position. The angle α is measured clockwise with respect to the x-axis starting from the cylinder stagnation point. The figure compares the results of the first-order scheme with those of the second-order scheme using a time step of 0.05. The two coefficients are depicted for four frequencies of $f_e/f_0 = 0.8$, 1.0, 1.1, and 1.2. The results of the second-order scheme are closer to the results of Guilmineau and Queutey [6] than to those of Yang and Balaras [38]. As is seen, the second-order scheme predicts better solutions at the stagnation, separation, and peak points. Considering a coarse mesh resolution, the predictions of the first-order scheme are reasonable except for the case of $f_e/f_0 = 1.0$.

Figure 12 shows the rms of the lift and drag coefficients and the time-averaged drag coefficient at four chosen frequencies studied in Figure 11. The results of the first-order scheme are compared with those of the second-order scheme at two time steps of 0.05 and 0.025. The magnitudes of the calculated coefficients are almost the same using the second-order scheme. The results of the first-order scheme approach the results of the second-order scheme as the time step decreases. The figure shows that the results of the second-order scheme are closer to those of Guilmineau and Queutey [6] than to those of Yang and Balaras [38].

The indentation wall problem is modeled as the third test case to show the accuracy and performance of our extended FVE-ALE in solving complex moving boundary problems. Figure 13 schematically shows the geometry of this test case. The motion of the indented wall, which is placed between x_2 and x_6 sections, is the same as those reported by Pedley and Stephanoff [39] and Demirdzic and Peric [3]. The height of the indented wall varies by time as follows:

$$y_w = y(x,t) = \begin{cases} 0 & \text{for } x < x_2 \text{ and } x > x_6 \\ 0.5h\{1 + \tanh[4.14(x - x_2 - x_a)]\} & \text{for } x_2 < x < x_3 \\ h & \text{for } x_3 < x < x_4 \\ 0.5h\{1 - \tanh[4.14(x - x_4 - x_a)]\} & \text{for } x_4 < x < x_6 \end{cases} \tag{34}$$

DOI: 10.1002/fld

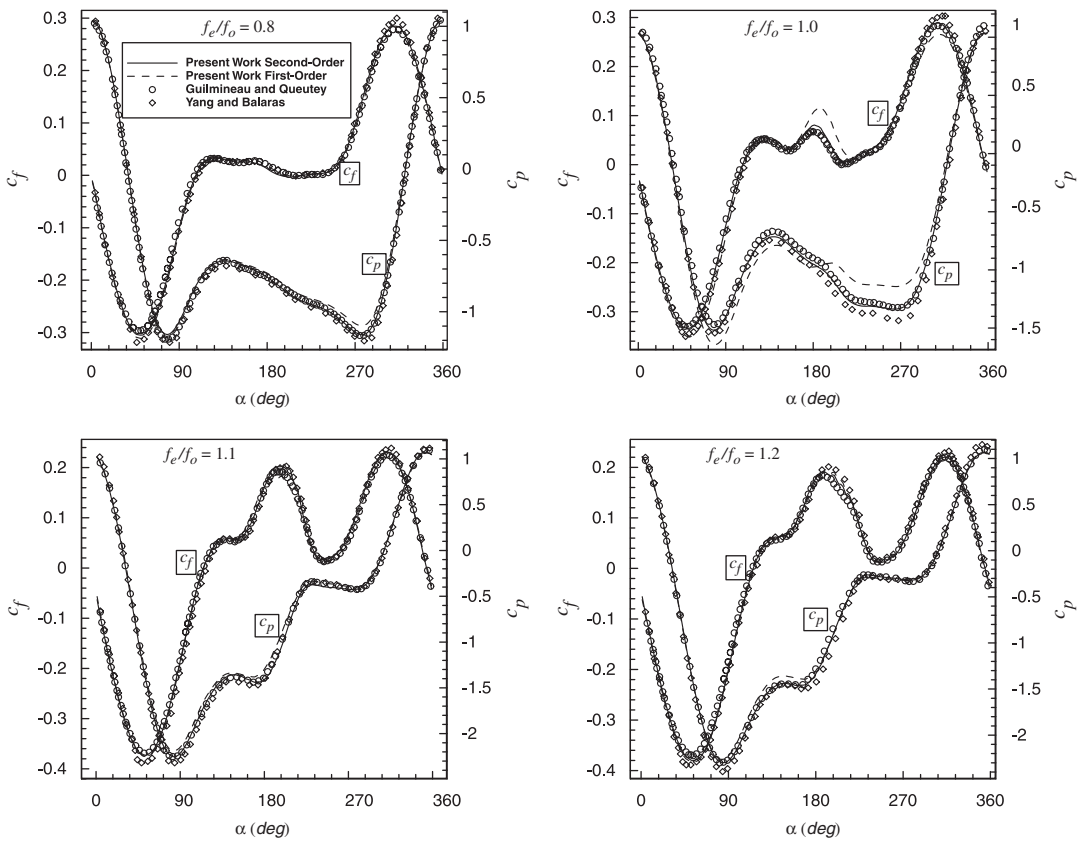

Figure 11. The present skin friction and pressure coefficient distributions around the transversely oscillating cylinder and comparing them with those of Guilmineau and Queutey [6] and Yang and Balaras [38], test 2.

where $h=0.5\varepsilon[1-\cos(2\pi T^*)]$ and $x_a=0.5(x_3-x_2)=0.5(x_6-x_4)$. The amplitude parameter ε indicates the maximum movement of the indented wall. The indentation period T is unity and time is non-dimensionalized using $T^*=t/T$. The inlet profile is parabolic and the mean value of the inlet velocity V_0 is unity. As the initial conditions, the longitudinal velocity and the pressure are considered unity, while the transversal velocity is zero. The height of the channel is $H=1$. The sizes of the computational domain are non-dimensionalized with respect to the channel height. The longitudinal positions are $x_1=0.0$, $x_2=3.35$, $x_3=5.85$, $x_4=13.85$, $x_5=15.1$, $x_6=16.35$, and $x_7=27.85$. The important parameters to specify this flow field are the Reynolds number, the Strouhal number, and the amplitude parameter. The Strouhal number St denotes the non-dimensional frequency of the indented wall. In this study, we consider Re$=507$, St$=0.037$, and $\varepsilon=0.38$.

Pedley and Stephanoff [39] described this test case and studied it both experimentally and theoretically. They found that the downstream flow field in the channel is quasi-steady for St<0.005. However, a train of waves propagates downstream of the channel for St>0.005 and closed eddies form in the separated flow field on the walls under their crests and above their troughs.

DOI: 10.1002/fld

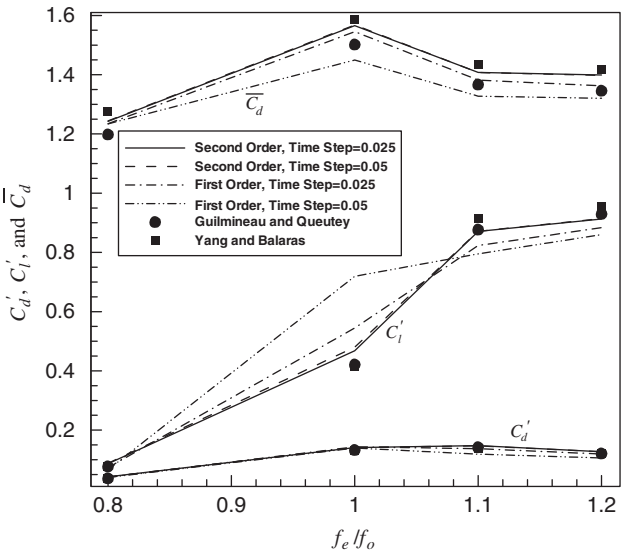

Figure 12. The rms and time-average of the lift and drag coefficients versus the frequency, compared with the results of Guilmineau and Queutey [6] and Yang and Balaras [38], test 2.

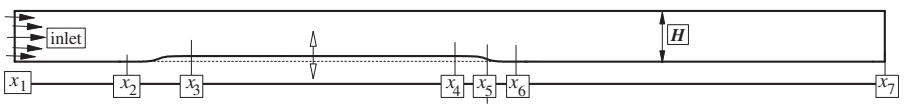

Figure 13. The geometry of a channel with an indented wall, test 3.

In addition, they found that the longitudinal positions of the vortex cores vary slightly with the Reynolds number. Ralph and Pedley [5, 40] simulated this problem via solving the stream function and vorticity equations with and without viscosity consideration. In order to resolve the moving boundary difficulties, they applied a time-dependent transformation. Using this transformation, they fixed their non-rectangular computational domain and applied an Eulerian approach to solve the flow field. They used two time steps of $\frac{1}{3200}$ and $\frac{1}{6000}$. Furthermore, Demirdzic and Peric [3] simulated this problem using the FV-ALE approach. They applied an implicit scheme and used two time steps of $\frac{1}{50}$ and $\frac{1}{200}$. They distributed 8840 nodes in their fine mesh. They further retained the orthogonality of their grids at the highest position. We perform our study for three hybrid mesh distributions having 4586, 8349, and 15 565 nodes in the domain. They are called coarse, moderate, and fine, respectively. Figure 1 shows a part of the coarse mesh distribution in the most sensitive part of the flow field at $T^*=0.0$, 0.3, and 0.4. This part is located around x_5 position, see Figure 13. As is observed, the quality of the mesh is quite suitable and there is no imperfect deformation in these three stages. The chosen time steps are $\frac{1}{20}$, $\frac{1}{50}$, $\frac{1}{100}$, and $\frac{1}{200}$. These four time steps are also called large, moderate, small, and fine time steps, respectively.

Figure 14 shows the propagation of the waves and the generation of the eddies along the channel and in downstream of the indented wall. These eddies are depicted at $T^*=0.4$, 0.5, 0.6, and

DOI: 10.1002/fld

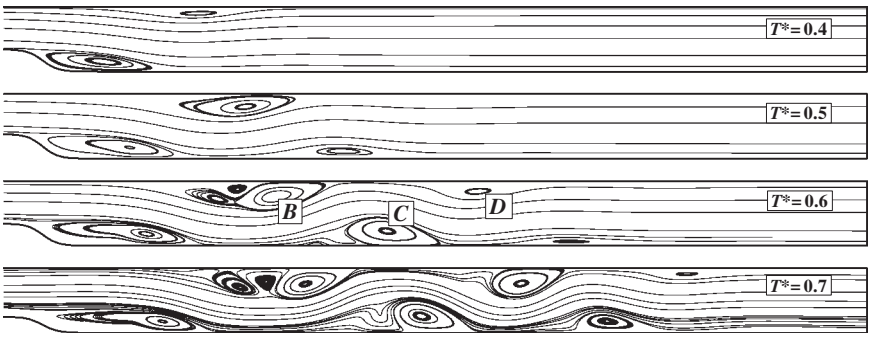

Figure 14. The eddy generation, propagation, and breakdown at different time levels, test 3.

0.7 using the instantaneous streamlines. The figure shows the trifurcation of the eddy B and the bifurcation of the eddy C at the chosen times. The details of eddy generation and propagation between the wave crest/trough and the walls are described in Ralph and Pedley [5, 40] and are not repeated here.

The best way to quantify the current results is to evaluate the positions of B, C, and D eddies, which are the most sensitive ones in the domain, see Figure 14. Figure 15 presents the details of comparison using the second-order time scheme. The two plots in this figure study the results of time step and grid resolution variations. Figure 15(a) presents the results of the moderate mesh at four large, moderate, small, and fine time steps. As is seen, decreasing the time step results in minor changes in the solutions. The results of using smaller time steps are always closer to the experimental data of Pedley and Stephanoff. The figure also presents the results of Demirdzic and Peric [3], who obtained their results using a time step of $\frac{1}{200}$ and a mesh resolution of 8840. They reported their eddy positions within some ranges. We have illustrated the mean values of their ranges in Figure 15. Using moderate time step and moderate mesh resolution, the current results provide better agreement with the experimental data than the numerical results of Demirdzic and Peric. Our method predicts the positions of the eddies B and C even better than those of Ralph and Pedley. However, they predict a better position for the eddy D. As is discussed in References [7, 40], the discrepancies can be originated from incipient 3D effects disturbing the experiment. These incipient 3D effects are more serious for the eddy D because of having weaker strength than the two other eddies. Ralph and Pedley used 30 000 nodes in the domain and they selected time steps smaller than $\frac{1}{3200}$. The figure also presents the results of Zhao and Forhad [7]. They used a grid with 51 217 nodes and 300 sub-iterations to derive their results. Generally, their accuracies are low compared with other demonstrated results. Figure 15(b) presents the results of using the small time step with three coarse, moderate, and fine meshes. As is seen, the mesh refinement has little influence on the solution. As is seen, the results of a finer mesh are always closer to the experimental data.

Figure 15 indicates that the current fine grid and fine time step solutions have converged to their limiting values. Additionally, compared with the experimental data, they are sufficiently accurate. If we assume that the fine grid and fine time step solutions are sufficiently accurate, we can compare the results of other coarser mesh resolutions and other larger time steps with these solutions and evaluate their relative accuracies. In this regard, Table III presents the relative accuracy of the first-order time accurate scheme and compares them with those of using the second-order scheme.

DOI: 10.1002/fld

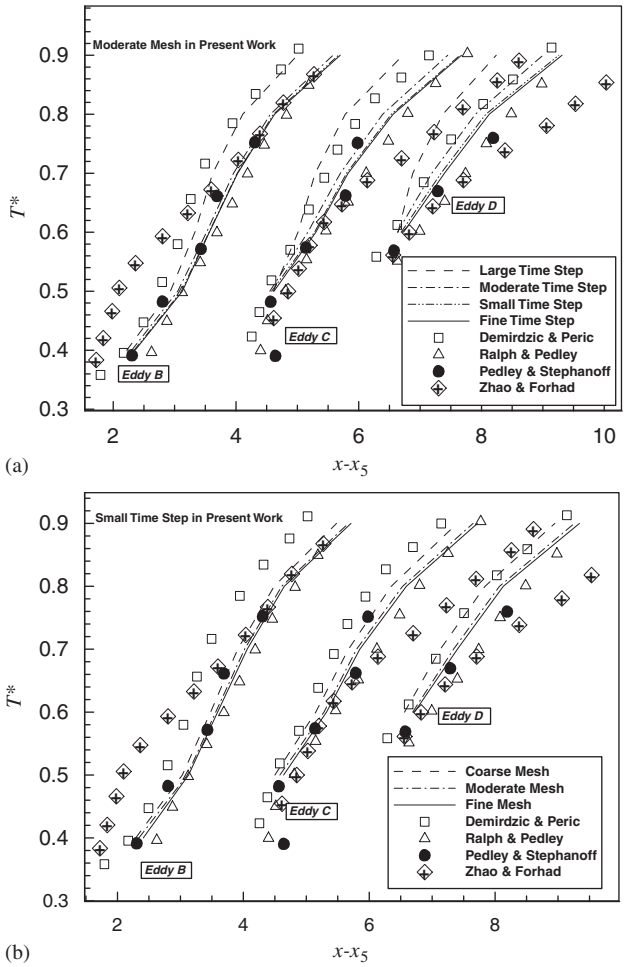

Figure 15. The positions of three eddies at different time steps (a) and various mesh node distributions (b) and comparison with the numerical results of Demirdzic and Peric [3], Zhao and Forhad [7], Ralph and Pedley [5, 40], and experimental data of Pedley and Stephanoff [39], test 3.

The relative accuracy is defined as the differences in the positions of B, C, and D eddies in each case with those predicted by the fine mesh and the fine time step. In other words, they are L_1-norm of the predicted positions of eddies relative to those of the fine mesh in the case of using the second-order time accurate scheme. The table presents the magnitudes in percentages considering a tolerance of 0.1%. The table indicates that the relative accuracies of the first-order scheme are more scattered than those of the second-order scheme. The relative accuracies of the second-order scheme at smaller time steps are nearly negligible. For example, the relative accuracies of the eddies C and D at $T^* = 0.6$ and 0.7 are small and nearly the same. As is seen in this table, the first-order scheme may not always converge to meaningful magnitudes for B, C, and D eddies. On the other hand, the relative accuracies in the second-order scheme decrease as the time step

DOI: 10.1002/fld

Table III. The comparison of the first-order and the second-order L_1-norms in predicting three eddy positions behind the indented wall, test 3.

Time accuracy →		First order			Second order		
		Eddy			Eddy		
$T^* \downarrow$	$\Delta t \downarrow$	*B*	*C*	*D*	*B*	*C*	*D*
0.6	$\frac{1}{50}$	1.6	0.2	2.1	1.3	2.6	1.5
	$\frac{1}{100}$	0.9	0.2	1.1	0.3	0.5	0.4
	$\frac{1}{200}$	0.2	0.0	0.5	0.0	0.0	0.0
0.7	$\frac{1}{50}$	3.8	2.9	0.8	1.7	2.2	2.8
	$\frac{1}{100}$	2.4	2.0	0.8	0.3	0.5	0.8
	$\frac{1}{200}$	1.2	1.5	0.7	0.0	0.0	0.0
0.8	$\frac{1}{50}$	4.0	3.8	2.2	1.6	2.8	2.6
	$\frac{1}{100}$	2.6	2.2	0.9	0.4	0.5	0.7
	$\frac{1}{200}$	1.5	1.0	0.4	0.0	0.0	0.0
0.9	$\frac{1}{50}$	—	—	—	2.0	3.1	3.5
	$\frac{1}{100}$	—	—	—	0.5	0.4	0.8
	$\frac{1}{200}$	—	—	—	0.0	0.0	0.0

deceases. The rate of relative accuracy decrease is steeper in the second-order scheme than that in the first-order scheme.

A careful study of the cell-face expressions shows that the diffusion terms are dominant at low Reynolds numbers but the convection terms are dominant at high Reynolds numbers. As was mentioned before, the pressure and diffusion terms are discretized using the FE shape functions; however, the convection terms benefit from a physical-influence upwind strategy. Therefore, the current method must be second-order accurate in low-Reynolds-number flows and first-order accurate in high-Reynolds-number flows. In addition, the temporal terms were separately discretized using either the first- or the second-order schemes. In order to perform the current temporal and spatial accuracies, we re-examine our chosen test cases.

First, we evaluate the spatial accuracy. In this regard, we consider four different uniform grids with 100×5, 200×10, 400×20, and 800×40 resolutions in the channel shown in Figure 13. We consider the results of 800×40 mesh as our reference magnitudes, because it is the finest mesh and includes all the other three meshes. The numerical study is performed at $T^* = 0.0$. The L_2-norm of pressure and velocity variables relative to those of the reference mesh is obtained and plotted in Figure 16(a) using the solid circle symbol. To present a better understanding of the current accuracy, the first- and second-order accurate slopes are also shown in this figure. Inspecting the figure, the slope of the pressure error is about 1.8, the longitudinal velocity about 1.2, and the transversal velocity about 1.3. The latter two magnitudes show that the convection role should be more dominant than the diffusion role in the channel at $\mathrm{Re} = 507$. The pressure error slope is close to 2. This is due to using a bilinear interpolation to approximate the pressure field in the domain. Our experience has shown that the second-order pressure accuracy would be achievable in solving other test cases as well.

DOI: 10.1002/fld

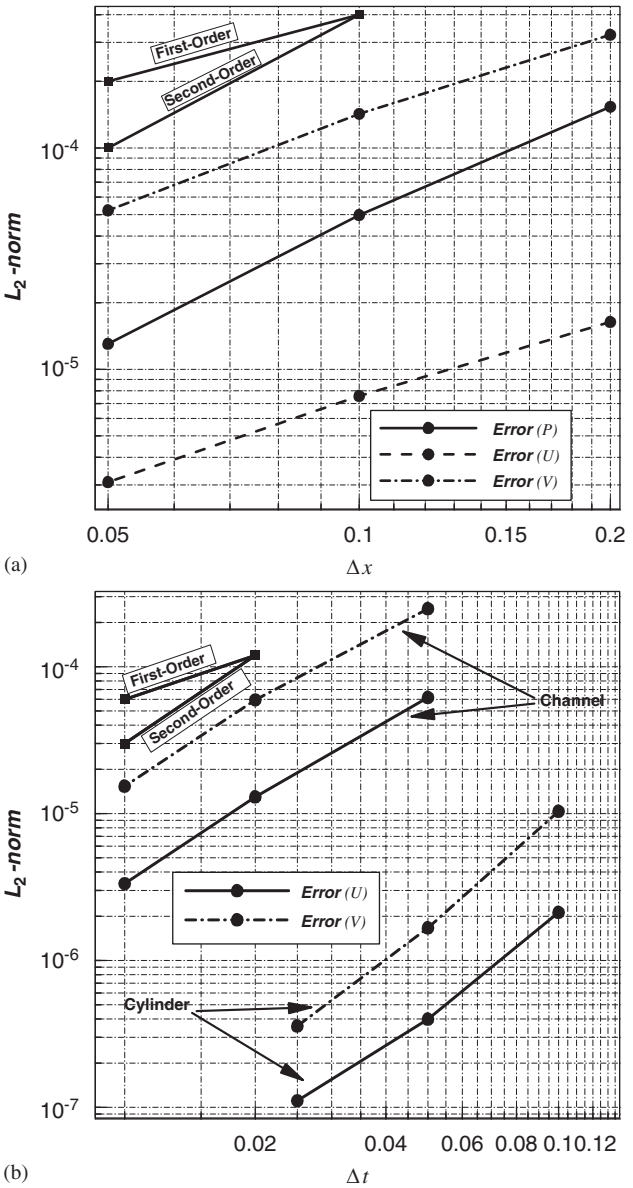

Figure 16. (a) Spatial accuracy study for test 2 with zero mesh velocities and (b) temporal accuracy study for tests 2 and 3.

Second, we evaluate the time accuracy. As the first step, we chose four different time steps of $\frac{1}{20}$, $\frac{1}{50}$, $\frac{1}{100}$, and $\frac{1}{200}$ with the moderate hybrid mesh to solve test 3. As before, the results at the finest time step are chosen as the reference magnitudes. We utilize the second-order time accurate scheme to study the problem and to obtain the magnitudes at $T^* = 0.6$. Figure 16(b) shows the

DOI: 10.1002/fld

L_2-norms of the velocity components and compares them with those of the reference slopes. As before, the solid squares show the second-order and first-order slopes in this figure. The slopes of the velocity error are very close to 2. At the second step, we re-examine the transversely oscillating cylinder test using the moderate mesh distribution. The study is performed at the moment when the cylinder is at the lowest position. The results show that the second-order accuracy has been achieved for both velocity components in this case as well. Consequently, we can conclude that the current method yields the second-order time accuracy when applying the second-order time stencil.

7. CONCLUSIONS

A primitive FVE method on stationary grids has been suitably extended to simulate unsteady flow in non-stationary grids benefiting from the ALE approach and satisfying the GCL. To enhance the accuracy of the method, the advection physics was carefully modeled using a physical-influence upwinding scheme on moving meshes. To elaborate the capability of the extended formulations, we examined both the first- and the second-order time accurate stencils. The accuracies of the current fluid flow and heat transfer solutions were evaluated in domains with zero mesh velocity, non-stationary domains, and domains with moving boundaries. Indeed, the current time step and grid resolution variations showed that the current method would predict reliable and accurate solutions despite using very coarse grid sizes and applying very large time steps in either stationary or non-stationary grids. Our investigation also showed that the time step in our extended formulations can be 10 times larger than those of other methods and that the accuracy of the current results is still comparable with their results. From grid size perspective, the number of grid nodes to provide accuracy comparable with the accuracy of other approaches was about one-tenth. These improvements can be attributed to the new hybrid method's exploitation of the strengths of FV, FE, and ALE techniques in a unified algorithm to solve the fluid flow and heat transfer problems in domains with moving grids. In our FVE-ALE approach, the second-order time accurate scheme established on fixed meshes yielded the second-order time accurate solutions on moving meshes.

REFERENCES

1. Zwart PJ, Raithby GD, Raw MJ. An integrated space–time finite-volume method for moving boundary problems. *Numerical Heat Transfer*, *Part B* 1998; **34**:257–270.
2. Zwart PJ, Raithby GD, Raw MJ. The integrated space–time finite-volume method and its application to moving boundary problems. *Journal of Computational Physics* 1999; **154**:497–519.
3. Demirdzic I, Peric M. Finite volume method for prediction of fluid flow in arbitrarily shaped domains with moving boundaries. *International Journal for Numerical Methods in Fluids* 1990; **10**:771–790.
4. Ahn HT, Kallinderis Y. Strongly coupled flow/structure interactions with a geometrically conservative ALE scheme on general hybrid meshes. *Journal of Computational Physics* 2006; **219**:671–696.
5. Ralph ME, Pedley TJ. Viscous and inviscid flow in a channel with a moving indentation. *Journal of Fluid Mechanics* 1989; **209**:543–566.
6. Guilmineau E, Queutey P. A numerical simulation of vortex shedding from an oscillating circular cylinder. *Journal of Fluids and Structures* 2002; **16**:773–794.
7. Zhao Y, Forhad A. A general method for simulation of fluid flows with moving and compliant boundaries on unstructured grids. *Computer Methods in Applied Mechanics and Engineering* 2003; **192**:4439–4466.
8. Zhang LP, Wang ZJ. A block LU-SGS implicit dual time stepping algorithm for hybrid dynamic meshes. *Computers & Fluids* 2004; **33**:891–916.
9. Zhang LP, Chang XH, Duan XP, Wang ZY, Zhang HX. A block LU-SGS implicit unsteady incompressible flow solver on hybrid dynamic grids for 2D external bio-fluid simulations. *Computers & Fluids* 2009; **38**:290–308.

DOI: 10.1002/fld

10. Dhatt G, Hubert G. A study of penalty elements for incompressible laminar flows. *International Journal for Numerical Methods in Fluids* 1986; **6**:1–19.
11. Fourestey G, Piperno S. A second-order time-accuracy ALE Lagrange–Galerkin method applied to wind engineering and control of bridge profiles. *Computer Methods in Applied Mechanics and Engineering* 2004; **193**:4117–4137.
12. Koobus B, Farhat C. Second-order time-accurate and geometrically conservation implicit schemes for flow computations on unstructured dynamic meshes. *Computer Methods in Applied Mechanics and Engineering* 1999; **170**:103–129.
13. Geuzaine P, Grandmont C, Farhat C. Design and analysis of ALE schemes with provable second-order time-accuracy for inviscid and viscous flow simulations. *Journal of Computational Physics* 2003; **191**:206–227.
14. Darbandi M, Schneider GE. Momentum variable procedure for solving compressible and incompressible flows. *AIAA Journal* 1997; **35**:1801–1805.
15. Darbandi M, Schneider GE. Analogy-based method for solving compressible and incompressible flows. *Journal of Thermophysics and Heat Transfer* 1998; **12**:239–247.
16. Rhie CM, Chow WL. Numerical study of the turbulent flow past an airfoil with trailing edge separation. *AIAA Journal* 1983; **21**:1525–1532.
17. Darbandi M, Bostandoost SM. A new formulation toward unifying the velocity role in collocated variable arrangement. *Numerical Heat Transfer*, *Part B* 2005; **47**:361–382.
18. Darbandi M, Naderi A. Multiblock hybrid grid finite volume method to solve flow in irregular geometries. *Computer Methods in Applied Mechanics and Engineering* 2006; **196**:321–336.
19. Darbandi M, Vakilipour S. Developing implicit pressure-weighted upwinding scheme to calculate steady and unsteady flows on unstructured grids. *International Journal for Numerical Methods in Fluids* 2008; **56**:115–141.
20. Darbandi M, Hosseinizadeh SF. Numerical simulation of thermobuoyant flow with large temperature variation. *Journal of Thermophysics and Heat Transfer* 2006; **20**:285–296.
21. Tannehill JC, Anderson DA, Pletcher RH. *Computational Fluid Mechanics and Heat Transfer*, Chapter 3. Taylor & Francis: Washington, DC, 1997.
22. Darbandi M, Schneider GE. Comparison of pressure-based velocity and momentum procedure for shock tube problem. *Numerical Heat Transfer*, *Part B* 1998; **33**:287–300.
23. Darbandi M, Vakilipour S. Using fully implicit conservative statements to close open boundaries passing through recirculations. *International Journal for Numerical Methods in Fluids* 2007; **53**:371–389.
24. Darbandi M, Schneider GE, Vakili S. Using different preconditioned Krylof subspace methods to solve coupled fluid flow equations. *CFD Journal* 2006; **15**:35–43.
25. Vakili S, Darbandi M. General recommendations to enhance the efficiency of algebraic multigrid preconditioned GMRES in solving coupled fluid flow equations. *Numerical Heat Transfer*, *Part B* 2009; **55**:232–256.
26. Posdziech O, Grundmann R. A systematic approach to the numerical calculation of fundamental quantities of the two dimensional flow over a circular cylinder. *Journal of Fluids and Structures* 2007; **23**:479–499.
27. Schlichting H. *Boundary-layer Theory*. McGraw-Hill: New York, 1979.
28. Henderson RD. Details of the drag curve near the onset of vortex shedding. *Physics of Fluids* 1995; **7**:2102–2104.
29. Lang C. Numerical prediction of heat and momentum transfer from a cylinder in cross flow with implications to hot-wire anemometry. *Ph.D. Thesis*, University Erlangen-Nurnberg, 1997.
30. De Sampaio PAB, Hallak PH, Coutinho ALGA, Pfeil MS. A stabilized finite element procedure for turbulent fluid–structure interaction using adaptive time–space refinement. *International Journal for Numerical Methods in Fluids* 2004; **44**:673–693.
31. Norberg C. Flow around a circular cylinder: aspects of fluctuating lift. *Journal of Fluids and Structures* 2001; **15**:459–469.
32. Williamson CHK, Roshko A. Measurements of base pressure in the wake of the cylinder at low Reynolds numbers. *Zeitschrift für Flugwissenschaften und Weltraumforschung* 1990; **14**:38–46.
33. Norberg C. An experimental investigation of the flow around a circular cylinder: influence of aspect ratio. *Journal of Fluid Mechanics* 1994; **258**:287–316.
34. White FM. *Viscous Fluid Flow*. McGraw-Hill: New York, 1991.
35. Eckert ERG, Drake RM. *Analysis of Heat and Mass Transfer*. McGraw-Hill: New York, 1972.
36. Karniadakis GE. Numerical simulation of forced convection heat transfer from a cylinder in crossflow. *International Journal of Heat and Mass Transfer* 1988; **31**:107–118.
37. Bouhairie S, Chu VH. Two-dimensional simulation of unsteady heat transfer from a circular cylinder in crossflow. *Journal of Fluid Mechanics* 2007; **570**:177–215.

DOI: 10.1002/fld

38. Yang J, Balaras E. An embedded-boundary formulation for large-eddy simulation of turbulent flows interacting with moving boundaries. *Journal of Computational Physics* 2006; **215**:12–40.
39. Pedley TJ, Stephanoff KD. Flow along a channel with time-dependent indentation in one wall: the generation of vorticity waves. *Journal of Fluid Mechanics* 1985; **160**:337–367.
40. Ralph ME, Pedley TJ. Flow in a channel with a moving indentation. *Journal of Fluid Mechanics* 1988; **190**:87–112.

DOI: 10.1002/fld